POLITECNICO DI TORINO
Repository ISTITUZIONALE

Numerical Cohesive Zone Modeling (CZM) of Self-Anchoring AM Metal-CFRP joints

Original
Numerical Cohesive Zone Modeling (CZM) of Self-Anchoring AM Metal-CFRP joints / Altunok, F.E., DE PASQUALE, G.. - In: FRATTURA E INTEGRITÀ STRUTTURALE. - ISSN 1971-8993. - 18:68(2024), pp. 280-295. [10.3221/IGF-ESIS.68.19]

Availability:
This version is available at: 11583/2989152 since: 2024-05-30T14:22:38Z

Publisher:
GRUPPO ITALIANO FRATTURA

Published
DOI:10.3221/IGF-ESIS.68.19

Terms of use:

This article is made available under terms and conditions as specified in the corresponding bibliographic description in the repository

Publisher copyright

(Article begins on next page)

10 November 2026

Numerical Cohesive Zone Modeling (CZM) of Self-Anchoring AM Metal-CFRP joints

Fikret Enes Altunok, Giorgio De Pasquale
Politecnico di Torino, Italy
fikret.altunok@polito.it, giorgio.depasquale@polito.it

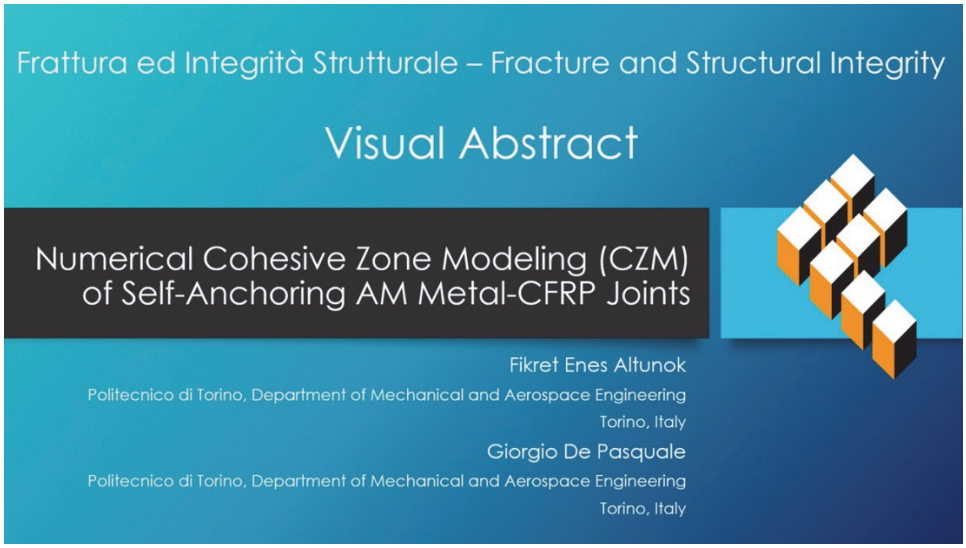

Citation: Altunok, F. E., De Pasquale, G., Numerical Cohesive Zone Modeling (CZM) of Self-Anchoring AM Metal-CFRP joints, Frattura ed Integrità Strutturale, 68 (2024) 280-295.

Received: 15.01.2024
Accepted: 09.02.2024
Published: 24.02.2024
Issue: 04.2024

Copyright: © 2024 This is an open access article under the terms of the CC-BY 4.0, which permits unrestricted use, distribution, and reproduction in any medium, provided the original author and source are credited.

KEYWORDS. Single-lap joints, Additive manufacturing, Composites, multimaterial joining, Cohesive zone modelling, Adhesives.

INTRODUCTION

In recent years, the imperative of achieving lightweight structures in engineering applications has gained increasing prominence, compelling researchers to explore novel methodologies to address this pivotal challenge. Khosravani et al. [1] conducted a meticulous investigation into the mechanical properties of single lap joints (SLJs) bonded with adhesives, utilizing 3D-printed PETG (polyethylene terephthalate glycol) adherents. The study, encompassing varied adhesive thicknesses and printing conditions, revealed cohesive failure as the predominant mode. Iwata et al. [2] delved into the joining process of aluminium and CFRP (carbon fiber reinforced polymer) sheets, examining the intricate influence of joining temperature on penetration rates for PA6 (polyamide-6) and carbon fibers within additively manufactured microstructures. The findings illuminated crucial insights into the nuanced factors affecting joint strength outcomes. Nguyen et al. [3] investigated the fracture toughness and adhesion characteristics of joints derived from L-PBF (laser powder bed fusion) generated Ti–Ti, as well as hybrid Ti-CFRP materials. Their exploration, utilizing mode I fracture toughness testing, unveiled altered fracture fronts when co-curing L-PBF surfaces with composite material. This deviation in failure patterns

underscored the intricate interactions between different materials in joint configurations. In the domain of adherent development, Parkers et al. [4] made notable strides by evaluating HYPER (hybrid penetrative reinforcement) joint designs with metal additive manufacturing (AM) techniques. Their comprehensive approach involved testing against varying interface circumstances, with the aim of comparing performance to an unanchored co-bonded reference. The results drew attention to the impact of employing a larger alternative anchor geometry in conjunction with a laser-treated interface, resulting in the most robust joint configuration. The laser treatment significantly altered the crack propagation rate, transitioning the failure mode from adhesive to cohesive—an essential revelation in the pursuit of durable joint configurations. Additional insights into joint configurations were provided by Neto et al. [5], who conducted a parametric analysis examining the length of the overlap zone in single-lap joints (SLJs). Their study revealed a direct relationship between failure load and extended overlap for SLJ composites bonded with a ductile adhesive. A consistent breakdown of cohesion within the ductile adhesive was observed, regardless of the overlap length. Conversely, when employing a brittle adhesive, saturation occurred notably beyond its 30 mm threshold upon implementing increased overlaps, underscoring the nuanced interplay between adhesive characteristics and joint configurations. Nash et al. [6] explored a novel implementation of adherents, specifically wavy sutures deviating from the conventional flat design. Their research delved into the distinctive configuration's capacity to significantly enhance shear stiffness in connections, with wavy sutures achieving an effective shear stiffness 10 to 20 times higher than the flat design. The angle of the wave critically influenced joint behavior, with set angles revealing distinctive effects on effective shear strength. This exploration expanded the repertoire of joint configurations, highlighting the potential of non-traditional designs in bolstering joint performance. Simultaneously, Ramaswamy et al. [7] embarked on a systematic approach to produce composite adherents with distinctive macro-scale interlocking properties. Their study investigated three distinct manufacturing procedures—simple-stacking, fiber-cutting, and moulding-in. Notably, among these strategies, the fiber-cutting method revealed striking characteristics, exemplifying the diverse avenues researchers are exploring to tailor adherent properties for specific applications. Within the realm of bonded/bolted joint analyses, Armentani et al. [8] utilized the finite element method (FEM) to assess the structural performance of single-lap hybrid systems. Their findings compared the stress distribution inside the adhesive layer of hybrid joints to that within exclusively adhesive-connected joints. The FEM analysis unequivocally established that the inclusion of a bolt substantially decreased shear stress in the adhesive layer. However, when considering peel stress—a different context altogether—a reduction in shear stress was not observed with bolted connections. This anomaly was attributed to limited compression action induced by preload within the range of the bolt head, providing nuanced insights into the multifaceted behavior of hybrid joints. The research landscape has been further enriched by Zhang et al. [9], who examined advancements in FEM analysis, specifically its application to composite hybrid joints (HJ). They categorized models into three main types, with a particular focus on the limitations of the elastic-plastic model in predicting performance before crack occurrence within adhesive bonds. Their primary emphasis on continuum damage modeling (CDM) and cohesive zone modeling (CZM) underscored the precision of these models in addressing hybrid failure modes. The integration of CDM and CZM formed a comprehensive strategy, enhancing calculation efficiency, especially when dealing with uncertain failure mechanisms in joints.

The array of methodologies and insights presented underscores the multifaceted nature of multimaterial joint modeling. This paper aims to address this challenge through an innovative approach to joining metal and composite parts, employing a series of anchors applied directly onto the metal adherent to facilitate the co-curing of the composite onto this substrate [10,11]. Specifically, alterations in the geometry of these anchors were considered as the primary factor influencing joint strength, and their effects were examined through numerical analysis, with a focus on employing the CZM method. Moreover, the design and optimization of such anchors are associated with the research domain of slender struts commonly found in lattice structures. This pertains to both the modeling aspect [12,13] and methodologies for experimentation [14].

MATERIALS AND METHODS

Geometries and mesh for numerical analysis

The geometric designs of anchors draw inspiration from those already described in [10]. While some geometries closely adhere to the original design for a direct comparison with those outcomes, others underwent slight adjustments or a complete overhaul.

The single-lap joint comprises two parts: the metal adherent and the CFRP (Carbon Fiber-Reinforced Polymer). Both adherents share identical dimensions, featuring a length of 40 mm, a width of 6 mm, and a thickness of 1.5 mm. The overlap at the interface between the adherents is 15 mm long, resulting in an overall length of 65 mm for the joined parts (Fig. 1).

The careful determination of specimen dimensions was integral to balancing computational efficiency with the need for accurate representation of the small-scale geometries of the anchors. To effectively observe anchor orientation effects and gradual joint separation, the width and length of the specimens were tailored to accommodate a minimum of two anchors and at least five anchors, respectively. This consideration stemmed from the intricate nature of the anchor geometries, necessitating the use of a small mesh element size to ensure precise representation. Consequently, any enlargement of the specimen dimensions would lead to a proportional increase in the number of elements required, thereby escalating computational demands and prolonging simulation time. Thus, the optimization of specimen dimensions played a critical role in minimizing computational costs while maintaining accuracy in the representation of the anchors' geometries. The anchors were designed with consistent dimensions; for example, those with a polygonal shape have an edge length of 1.5 mm, while those with circular anchors have a diameter of 1.5 mm. All anchors have a uniform height of 1.25 mm. Each joint includes 10 anchors positioned at a distance of 1.5 mm from each other and at a distance of 0.75 mm from the joint edges (Fig. 1). This design aims to minimize the variability of results attributable to anchor size and positioning, primarily reflecting the geometry of the anchors. Fig. 2 illustrates the metal part of the joint with the anchor geometries investigated in the subsequent modeling activity. The properties of the adherent materials (Inconel 625 and long fiber composite) are obtained from [10] and documented in Tab. 1.

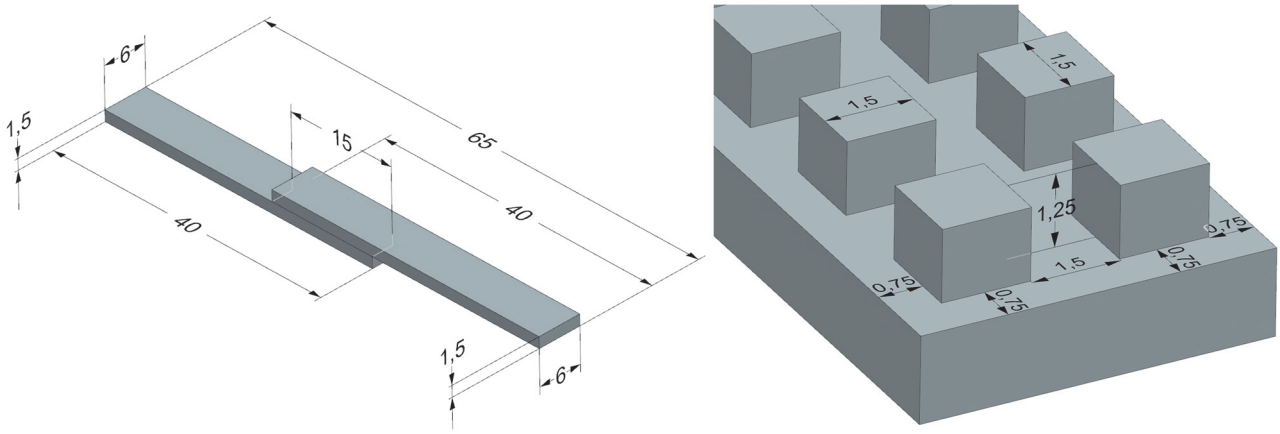

Figure 1: Dimensions (in millimeters) of the joint and anchors.

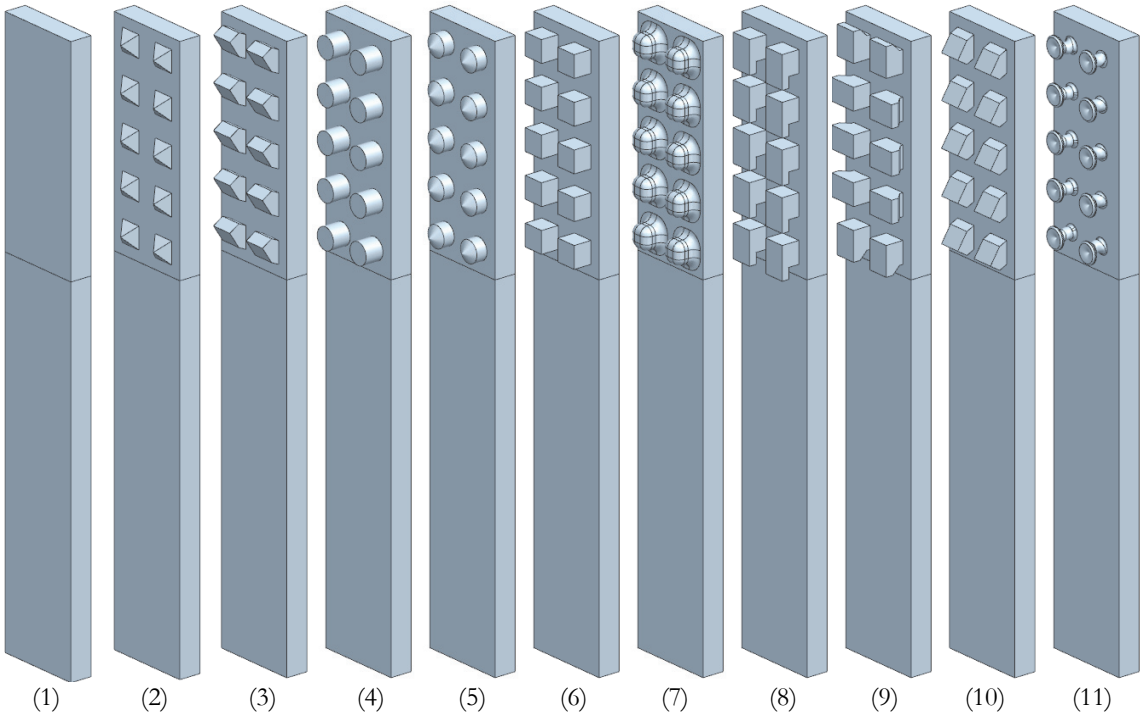

Figure 2: Metal side of the joint with different anchor geometries: 1) Plain, 2) Pyramid, 3) Reverse Spike, 4) Cylinder, 5) Cylinder Chamfered, 6) Block, 7) Rounded Block, 8) L-Block, 9) Edge Overhang, 10) Spike, 11) Gecko.

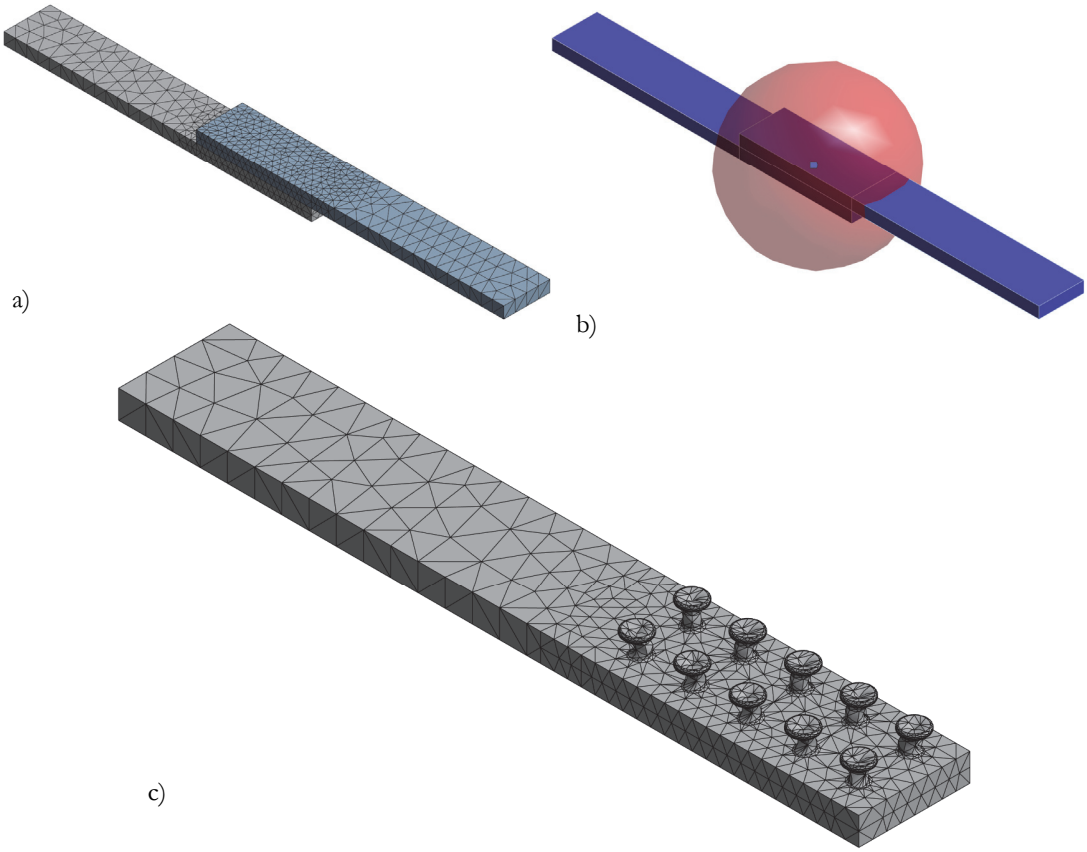

Figure 3: Mesh used for specimens of the CZM simulations (a), spherical sizing mesh refinement applied to bodies (b), detail view of an example mesh on a geometry with Gecko anchors (c).

All geometries featuring different anchors adhere to same approach in meshing (see Fig. 3a), wherein a refinement strategy is employed primarily within the overlap region to ensure precise representation. Across all geometries, a consistent refinement method was implemented, involving the selection of a spherical region with a diameter of 10 mm to dictate mesh element size (as illustrated in Fig. 3b). While maintaining a global element size of 1.5 mm, this localized refinement zone necessitated a reduced element size of 0.75 mm. To accommodate the intricacies of the anchors' geometrical features, software-controlled adaptive mesh sizing was activated, empowering the ANSYS meshing tool to dynamically adjust element size for regions where anchor features exceeded the predetermined element size threshold. This adaptive approach ensured the accurate representation of even the most complex anchor structures (depicted in Fig. 3c).

Inconel 625		CFRP	
E (MPa)	180000	$E_x = E_y$ (MPa)	35000
		E_z (MPa)	3000
G (MPa)	69230	$G_x = G_y$ (MPa)	1154
		G_z (MPa)	1154
ν	0.3	$\nu_{xy} = \nu_{xz} = \nu_{yz}$	0.3

Table 1: Properties for Inconel 625 and CFRP [10].

Mesh sensitivity analysis

A mesh sensitivity study was conducted on the "Block" geometry using Araldite2015 as the adhesive. The most pertinent parameter considered is the maximum reaction force obtained at the constrained end throughout the simulation,

representing the joint failure load. The results of the sensitivity analysis are listed in Tab. 2 and represented in Fig. 4. A 0.75 mm element size was determined as the optimal compromise between solution accuracy and computation time.

Element size (mm)	3	1.5	0.75	0.375	0.1875
Number of Elements	1708	2974	9464	60 238	553 015
Solution Time	48s	1m 37s	22m 28s	2h 18m 50s	1d 13h 19m
Reaction Force (N)	3503.3	3498.9	3287.0	3097.9	3095.7

Table 2: Simulation results at different mesh element sizes.

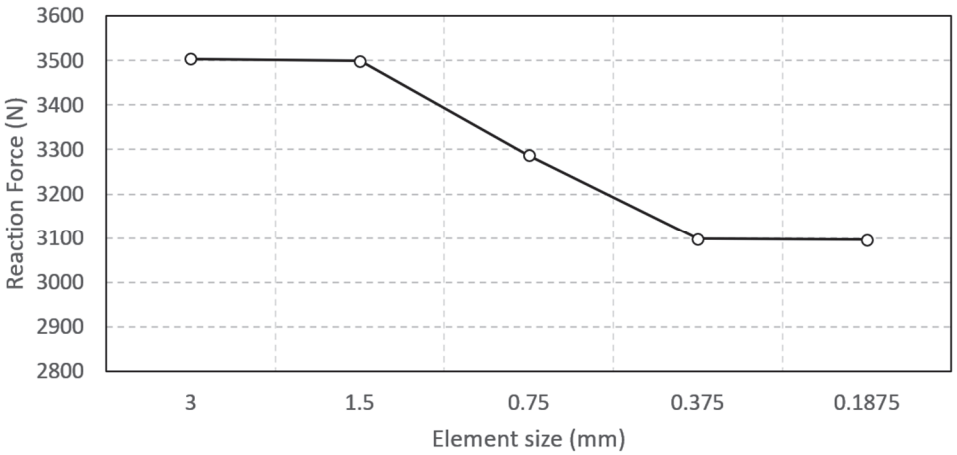

Figure 4: Mesh sensitivity analysis.

THE COHESIVE ZONE MODELLING (CZM)

In order to forecast the strength of joints with different anchor geometries, it is imperative to accurately simulate the joint failure mechanism. One such failure is cohesive failure, wherein the single-lap joint experiences complete separation due to a failure in the connection area inside the bond itself. In this mode, the cohesive strength of the adhesive is surpassed, leading to the achievement of maximum joint strength.

In the analysis, the overlap region between two adherents was treated as a contact surface, integrating a damage model known as the Cohesive Zone Model (CZM) between each set of nodes. The proposed modeling technique utilized ANSYS 2023 R2 Mechanical's contact debonding tool. Establishing the correct parameters for cohesive zone properties of materials was essential to ensure the method's effectiveness without encountering convergence issues and to achieve accurate results. This technique introduces a fracture mechanism by adopting loading-softening relationships between traction and separation, based on the assumption of a critical fracture energy.

The definitions of the traction and separation relationship depend on the element and material model, adopting either an exponential or a bilinear material model behavior. For the bilinear model, the selected method can be based on the dominating separation behavior, encompassing Mode-I, Mode-II, or mixed-mode debonding. In Mode-I, the predominant displacement jump is normal to the surfaces, while in Mode-II, it is mainly tangential. Mixed mode involves both tangential and normal displacements, significantly affecting separation.

This study employed the bilinear mixed-mode traction-separation law, and the cohesive zone properties were defined accordingly. Fig. 5 illustrates the qualitative shape of the relationship between contact stress and contact gap for a bilinear cohesive zone material.

The diagram illustrates linear elastic loading (0A) followed by linear softening (AC). Point A marks the culmination of linear elastic loading, achieving the maximum contact stress and contact gap "u." The initiation of debonding occurs at point A, with "d" denoting the debonding parameter, and concludes at point C. Subsequent separation occurs without any contact stress. The region beneath the curve represents the critical fracture energy, i.e., the energy released during contact debonding.

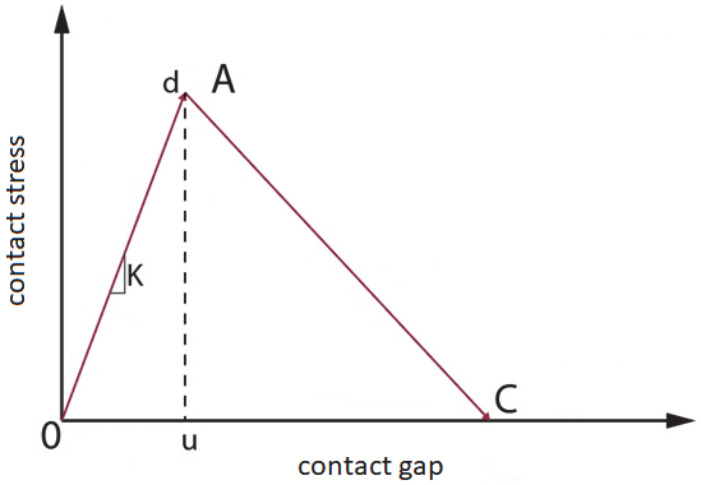

Figure 5: Bilinear traction-separation law applied to the CZM model of the joint.

The slope of the 0A segment determines the contact gap at the maximum contact stress, providing insights into how the contact stress diminishes with the contact gap. This characterization also discerns whether the fracture is ductile or brittle. In the case of mixed-mode debonding, the debonding process is influenced by both normal and tangential contact stresses.

$$Normal\ stress: P = K_n u_n \left(1 - d\right) \tag{1}$$

$$Tangential\ stress: \tau = K_t u_t \left(1 - d\right) \tag{2}$$

where K_n and K_t are the normal and tangential elastic contact stiffness before debonding, u_n and u_t are the normal and tangential gaps where debonding starts. In the context of mixed-mode debonding, both normal and tangential contact stresses play a role in the overall fracture energy. Debonding is concluded before reaching the critical fracture energies for the components. Hence, a unified energy criterion is employed to delineate the conclusion of debonding:

$$\left(\frac{G_n}{G_{cn}}\right)^{\frac{\alpha}{2}} + \left(\frac{G_t}{G_{ct}}\right)^{\frac{\alpha}{2}} = 1 \tag{3}$$

where:

$$G_n = \int P du_n \tag{4}$$

$$G_t = \int \tau du_t \tag{5}$$

G_n and G_t represent the normal and tangential fracture energies, while G_{cn} and G_{ct} denote the fracture energies at the conclusion of debonding. The power law exponent α, governing mixed-mode debonding, is disregarded (α = 2).

Validation of the CZM on Single-Lap Joints (SLJ)

To evaluate the effectiveness of the described CZM method in static structural analysis, a validation study was undertaken. The reference considered for this validation is the study by Carvalho and Campilho [15], who conducted a specific investigation on adhesive simulations. Their research involved the analysis of tensile test specimens, comprising single lap joint (SLJ) structures made of ductile aluminum AA6082 T651 with flat joint surface. The geometric dimensions and material properties of the specimens are directly adopted from their investigation and incorporated into the CZM simulation using ANSYS 2023 R2. The geometry featured a simple SLJ configuration, with no modifications to the adherent surfaces, as depicted in Fig. 6. For all specimens, the total joint length was set at 170 mm, the width was 25 mm while the thickness of each adherent was always 3 mm. The length of overlap zone was changing between specimens with values as 12.5 mm, 25 mm, 37.5 mm and 50 mm.

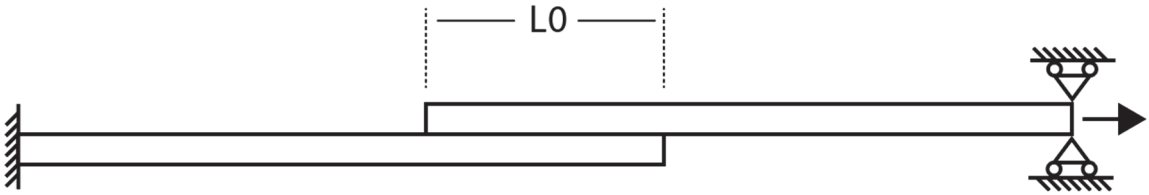

Figure 6: Geometrical and structural description of the specimen used in the validation study.

In the referenced study, the performance of three adhesives—Araldite® AV138, Araldite® 2015, and SikaForce® 7752—was examined. The Cohesive Properties of these adhesives were detailed in Tab. 3, these properties were used to define material cards in Engineering Data module of ANSYS by computing the Separation-Distance Based Debonding properties according to the equations for the specific element used. The adherents of the joints are composed of Aluminum AA6082 T651, with the properties outlined in Tab. 4.

Upon establishing the material data and geometric parameters, simulations were executed utilizing the ANSYS 2023 R2 Mechanical module. When generating the mesh, the primary focus in the simulations is directed towards refining the bonded region. Indeed, the influence of mesh size on other parts of the structure is relatively less important in the assessment of outcomes, considering that during tensile testing, the bonded area experiences a bending moment due to its asymmetric configuration. This phenomenon results in the concentration of tension at the boundaries of the bonded region, emphasizing the significance of the overlap zone and underscoring the need for a less detailed mesh elsewhere.

To maintain consistency with the original study, the boundary conditions were set to ensure a true representation of a tensile test. Referring to Fig. 6, the specimens are fixed at one end, while a displacement of 1 mm in the positive "X" direction is applied to the opposite end. The mesh comprises hexahedral elements, where an element size of 2 mm is assigned to the overlapping region. The overall element size remains unchanged at its default setting. (Fig 7)

Property	Unit	Araldite® AV138	Araldite® 2015	SikaForce® 7752
Young's modulus	GPa	4.9 ± 0.8	1.9 ± 0.2	0.5 ± 0.1
Poisson's ratio	-	0.35	0.33	0.30
Tensile yield stress	MPa	36.5 ± 2.5	12.6 ± 0.6	3.2 ± 0.5
Tensile failure strength	MPa	39.5 ± 3.2	21.6 ± 1.6	11.5 ± 0.3
Tensile failure strain	%	1.2 ± 0.1	4.8 ± 0.8	19.2 ± 1.4
Shear modulus	GPa	1.6 ± 0.01	0.6 ± 0.2	0.2 ± 0.01
Shear yield s tress	MPa	25.1 ± 0.3	14.6 ± 1.3	5.2 ± 1.1
Shear failure strength	MPa	30.2 ± 0.4	17.9 ± 1.8	10.2 ± 0.6
Shear failure strain	%	7.8 ± 0.7	43.9 ± 3.4	54.8 ± 6.4
Toughness in tension	N/mm	0.20 ± 0.2	0.4 ± 0.02	2.4 ± 0.2
Toughness in shear	N/mm	0.38 ± 0.2	4.7 ± 0.3	5.4 ± 0.5

Table 3: Cohesive properties of the materials reported in [15].

Property	Unit	Aluminum AA6882 T651
Young's modulus	GPa	70.0
Poisson's ratio	-	0.33
Tensile yield stress	MPa	265
Tensile ultimate stress	MPa	324
Bulk modulus*	GPa	68.6
Shear modulus*	GPa	26.3

Table 4: Properties of Aluminum AA6082 T651 (* derived from Young's Modulus and Poisson's Ratio: Online Materials Information Resource – MatWeb).

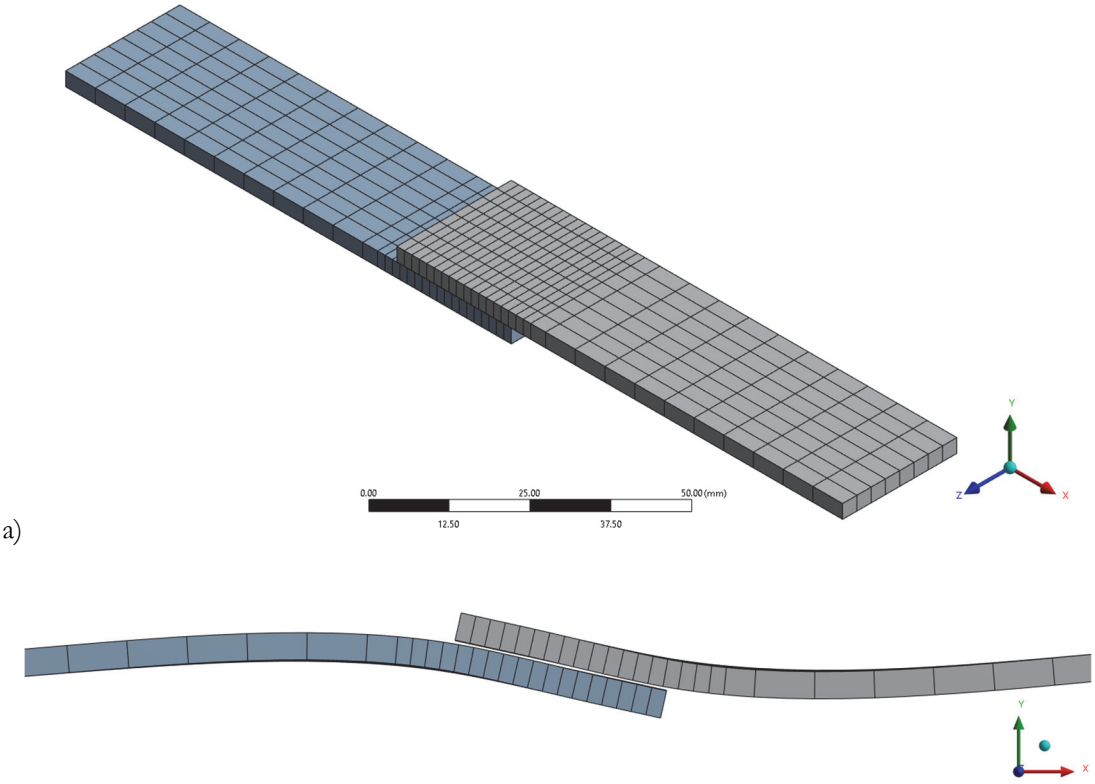

a)

b)

Figure 7: Mesh of the specimen for validation study (a) and the detail of the last CZM simulation step with complete separation of adherents, scaled up to 8.5x for better visualization (b).

In the simulations, CZM was utilized, incorporating the Contact Debonding fracture definition within the simulation software. In the validation study, the length of the overlap zone (L0) of the SLJ was identified as a key variable. Subsequently, a series of CZM simulations were conducted, varying this length among specimens bonded with different adhesives.
Joint failure is characterized by the complete separation between adherents. The detachment point denotes the maximum load-bearing capacity of the joint, representing the maximum load each specimen and adhesive can withstand before failure. The simulation results are presented in Tab. 5 and Fig. 8.

Overlap length L0 (mm)	Failure load (N)		
	Araldite® AV138	Araldite® 2015	SikaForce® 7752
12.5	5258.1	4284.8	3849.5
25.0	6645.0	8748.8	7503.1
37.5	7927.0	12054.0	10843.0
50.0	9186.2	15491.0	14252.0

Table 5: Failure loads calculated with the CZM on SLJ depending on different adhesives at variable lengths of the overlap (L0) between the bonded adherents.

Examining the simulation results depicted in Fig. 8, the observed trend suggests that as the length of the overlap region increases, there is a proportional increase in the joint's resistance, quantified by the failure load. Importantly, the outcomes obtained from CZM simulations closely align with the experimental parameters documented [15], demonstrating a robust correlation (see Tab. 6). This observation underscores the reliability and precision of the methodology applied in this study for assessing the performance of adhesively bonded SLJ using the CZM.

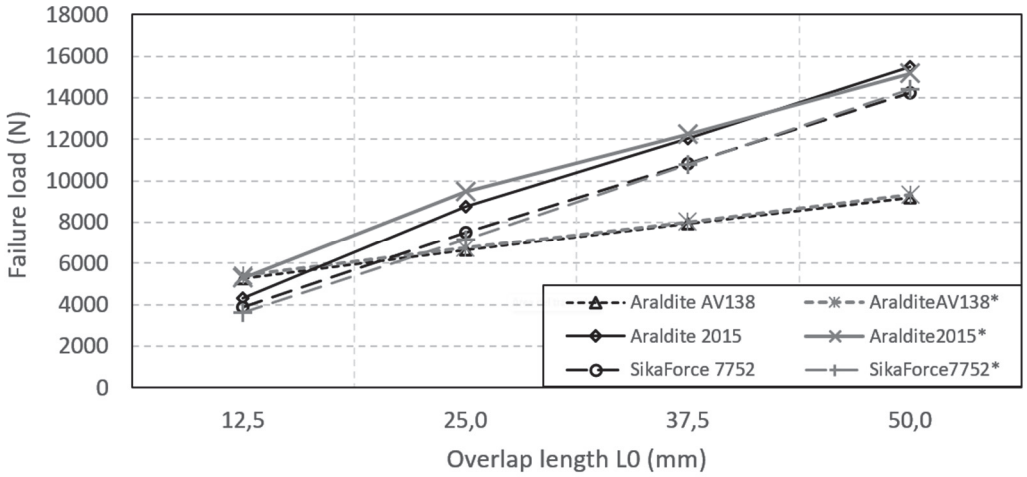

Figure 8: Comparison between experimental results (marked with * symbol) [15] and simulation results based on CZM.

	% Error in Failure Load between CZM and Experiment [15]		
L0 (mm)	AralditeAV138	Araldite2015	SikaForce7752
12.5	-2.95%	-18.89%	6.09%
25.0	-1.32%	-7.70%	4.60%
37.5	-1.12%	-1.46%	0.62%
50.0	-1.75%	2.01%	-0.97%

Table 6: Percentage error between CZM simulations and Experiment [15].

RESULTS AND DISCUSSIONS

Debonding simulations were conducted for the eleven distinct joint geometries illustrated in Fig. 2. The reaction force at the fixed end of each joint was also computed. Notably, this force reaches its peak value concurrently with joint failure. To ensure comparability among anchor geometries and mitigate the influence of specific adhesives, the three different adhesives outlined in Tab. 3 were considered in the simulations. Certain geometries, such as Plain, Pyramid, Reverse Spike, Cylinder, Cylinder Chamfered, Block, and Rounded Block, demonstrate complete separation in the joints. The calculated values of failure loads for joints with these anchor geometries are presented in Tab. 7.

Among all the joints, except for the Plain geometry, SikaForce® 7752 consistently resulted in the highest failure load for all anchor geometries, contributing to a more robust connection. Conversely, joints employing Araldite® AV138 consistently demonstrated the weakest performance. Examining the anchor types, as depicted in Tab. 7, the Block geometry consistently attained the highest failure load across all three adhesives, establishing it as the most robust joint design.

Among the eleven anchor geometries considered, for some geometries, namely L-block, Edge Overhang, Spike, and Gecko, complete separation was not observed. This result can be attributed to the shapes of these designs, allowing for enhanced mechanical interlocking. Geometries that undergo complete separation exhibit a peak value in their force reaction-displacement curve, corresponding to the failure load. In contrast, those without complete separation do not reach a maximum load value on the same curve.

Upon scrutinizing the contact status results, it was observed that separation consistently initiates from the free-end side of the overlap region and propagates toward the fixed-end side. In the simulations, the complete separation of adherents occurs when the contact status of nodes on the overlap region changes. Initially, in ANSYS 2023 R2 Mechanical, the nodes of the contact element assignment are set to "sticking." As the load increases, the status changes to “sliding,” “near,” or “far,” depending on the distance with the target surface, in accordance with default or user-defined thresholds.

Anchor Geometry	Failure Load for Different Adhesives (N)		
	Araldite® AV138	Araldite® 2015	SikaForce® 7752
Plain	1177	1230	1201
Pyramid	1193	1195	1542
Reverse Spike	1397	1844	2490
Cylinder	1860	2561	3327
Cylinder Chamfered	1662	2299	4215
Block	2143	3287	4990
Rounded Block	1468	1810	3765

Table 7: Failure load from the joint simulations depending on the adhesive type for the anchor geometries showing complete separation.

The contact status results for each anchor geometry are presented for the Araldite® AV138 adhesive, distinguishing between joints where separation was observed (Tab. 8) and those where it was not observed (Tab. 9). The contact status of each element is delineated through a color-coded representation.

An important observation is that the maximum load of the joint is consistently attained before complete separation occurs, typically after the propagation of separation passes the second row of anchors from the free-end side. Based on this observation, the load value calculated at the constrained end when separation propagates just after the second row of anchors was arbitrarily assumed as the "assumed failure" load.

For geometries undergoing complete separation, this "assumed failure" can be compared with the "failure load" already reported in Tab. 7. Subsequently, the loads at complete separation consistently fell within the range of failure loads, resulting in a maximum error of 8% (Tab. 10). This outcome suggests that the load at "assumed failure" can serve as a reliable comparative metric for joint strength.

Anchor Geometry	Contact Status at Failure	Contact Status at Complete Separation
Plain	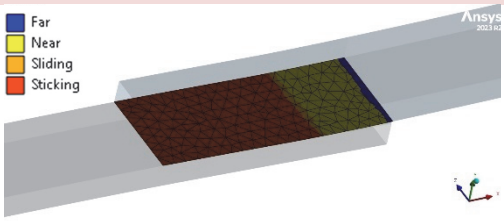	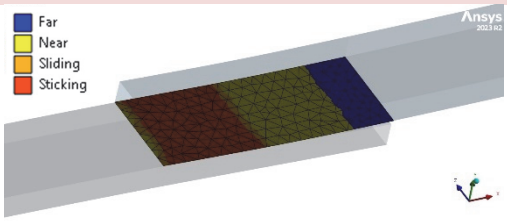
Pyramid	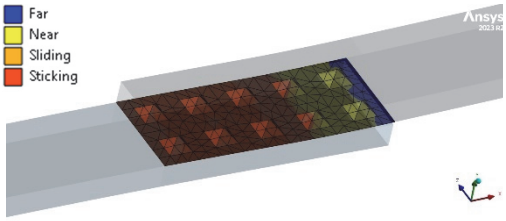	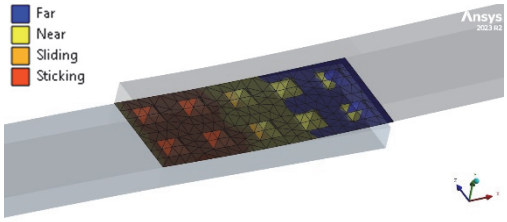
Reverse Spike	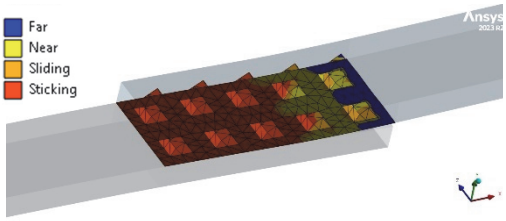	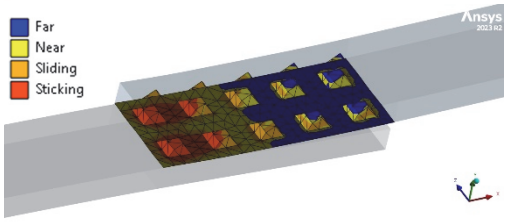
Cylinder	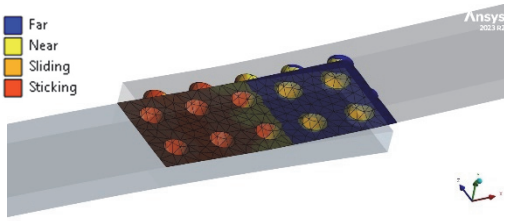	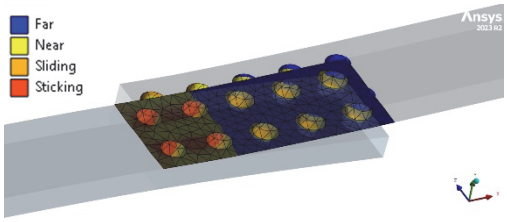
Cylinder Chamfered	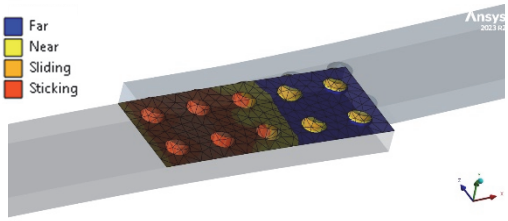	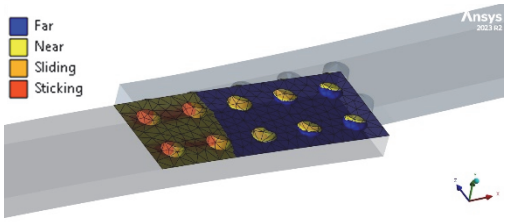
Block	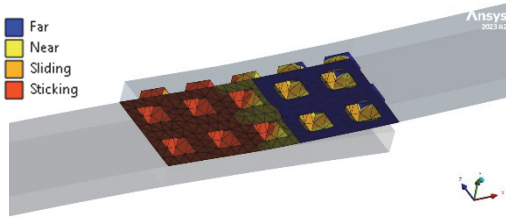	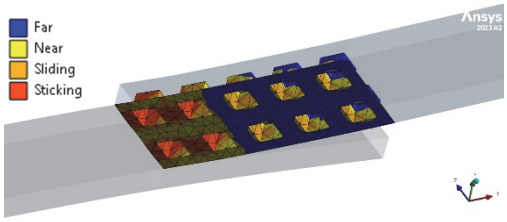
Rounded Block	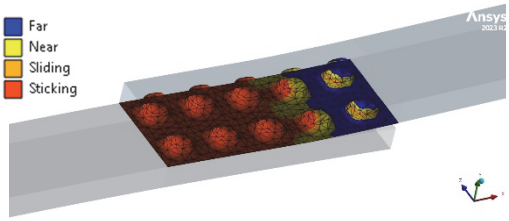	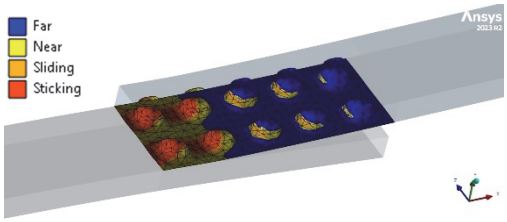

Table 8: Images representing the contact status results for different anchor geometries where the complete separation was observed. Adhesive: Araldite® AV138. Contact status: far (blue), near (yellow), sliding (orange), sticking (red).

Anchor Geometry	Contact Status at Assumed Failure	Contact Status at Complete Separation
L-Block	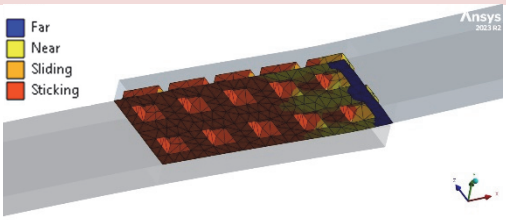	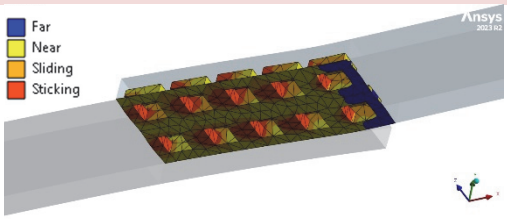
Edge Overhang	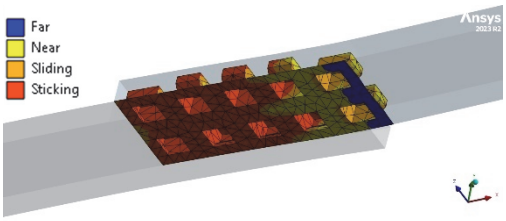	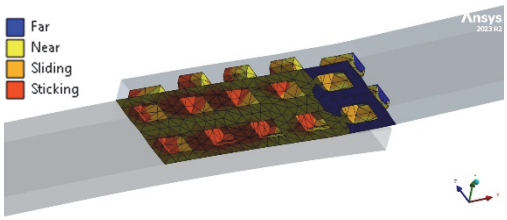
Spike	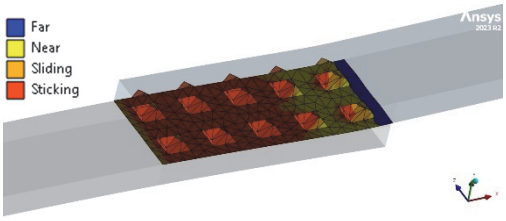	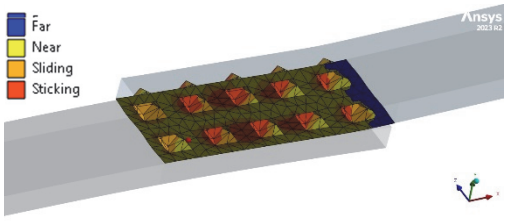
Gecko	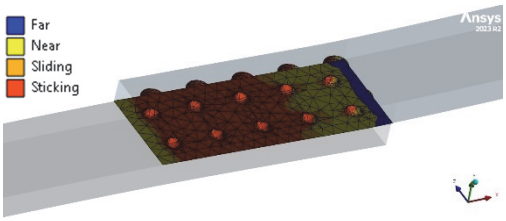	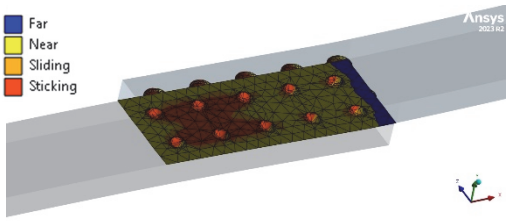

Table 9: Images representing the contact status results for different anchor geometries where the complete separation was not observed. The "assumed failure" refers to the separation propagation placed just beyond the second anchors row. The "complete separation" refers to change of nodes status from "sticking" to a different assignment. Adhesive: Araldite® AV138. Contact status: far (blue), near (yellow), sliding (orange), sticking (red).

Anchor Geometry	Complete Separation Load (N)	Failure Load (N)	Difference (%)
Plain	1100	1177	7%
Pyramid	1133	1193	5%
Reverse spike	1336	1405	5%
Cylinder	1737	1860	7%
Cylinder chamfered	1545	1662	7%
Block	2040	2143	5%
Rounded Block	1348	1468	8%
L-Block*	3827 (1)	2722 (2)	-41%
Edge Overhang*	4282 (1)	3109 (2)	-38%
Spike*	3250 (1)	2362 (2)	-38%
Gecko*	2393 (1)	2272 (2)	-5%

Table 10: Joint strength loads for different geometries for Araldite® AV138. (*) Anchor geometries not exhibiting complete joint separation. (1) Load when the contact status on the overlap region nodes changes from "sticking" to a different assignment. (2) Load when the contact status change is observed passed the second set of anchors, "Assumed Failure".

The force reaction-displacement curves depicting joints experiencing complete separation were presented in Fig. 9. For comparative analysis of different anchor geometries, the maximum force reaction value was identified as the failure load. Notably, failure was not equated with complete separation, as the reaction load at complete separation consistently appeared lower. Hence, it was presumed that joint failure occurred prior to complete separation. Conversely, for joints not undergoing complete separation, corresponding force reaction-displacement curves were depicted in Fig. 10. As previously noted, these curves lacked a distinct maximum point due to the absence of complete separation. The failure load for such geometries was approximated as the load at which separation extended beyond the second set of anchors.

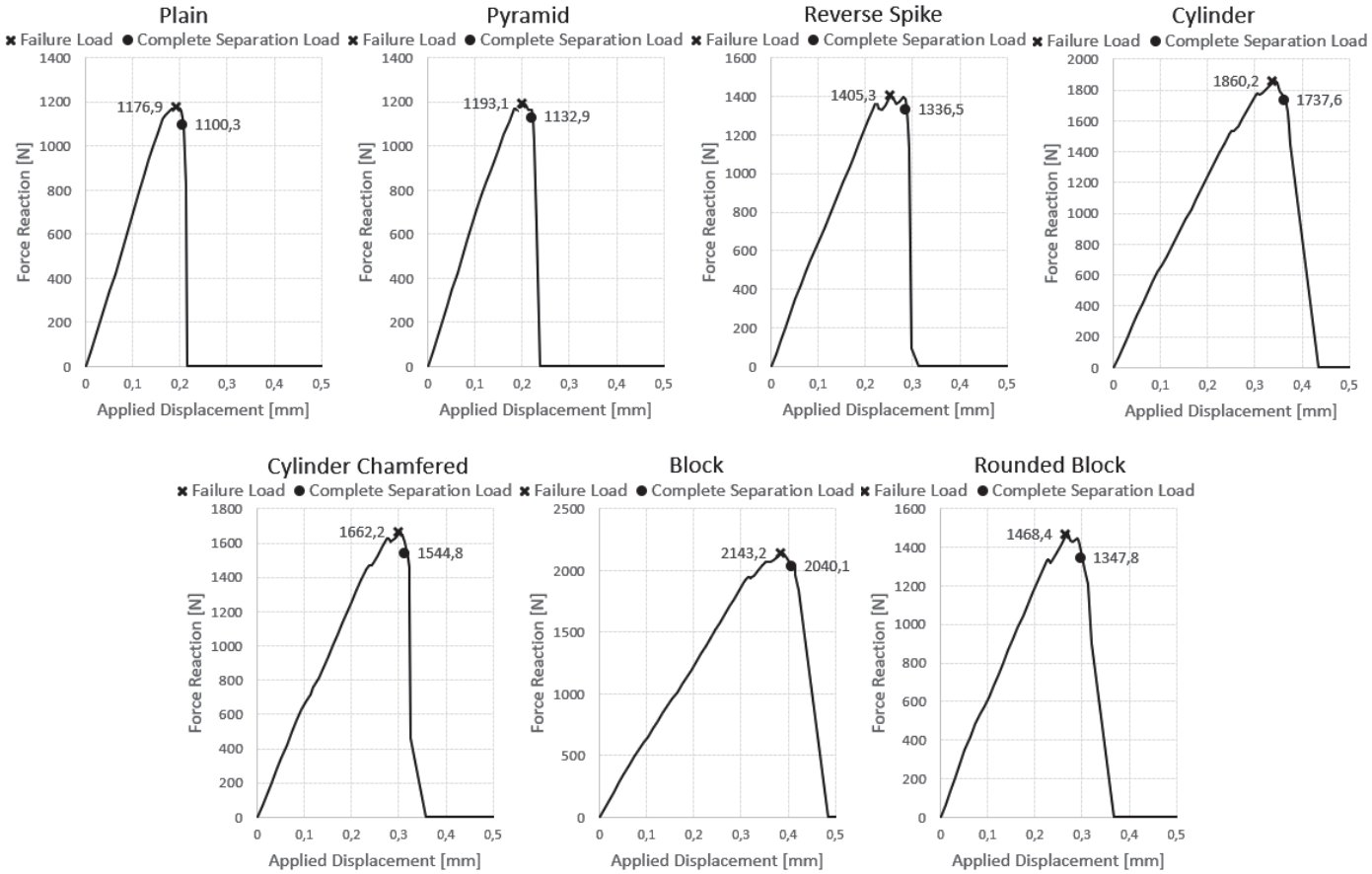

Figure 9: Force Reaction – Displacement curves for the geometries where a complete separation was observed.

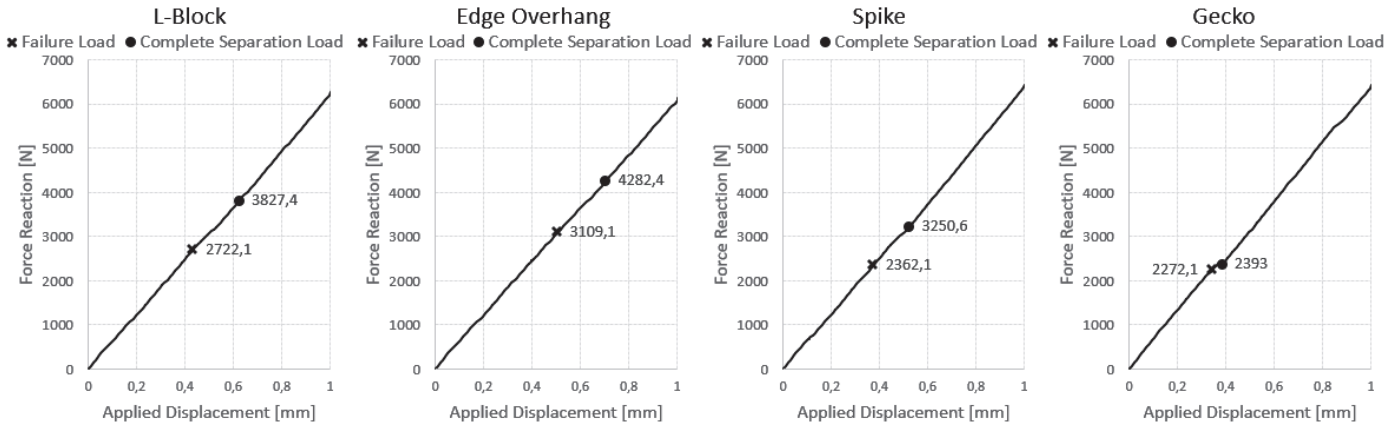

Figure 10: Force Reaction – Displacement curves for the geometries where a complete separation was not observed.

In particular, for geometries where failure is not observable, the load at complete separation provides valuable insights. Based on this assumption, for these joints, the "assumed failure" is associated with the moment when separation extends

beyond the second anchor rows, while the "complete separation load" is computed when the contact status of the nodes on the horizontal faces of the overlap region changes from "sticking" to a different assignment. as reported in Tab. 9, and the corresponding load value is calculated. The values of complete separation loads are presented in Tab. 10 alongside the failure loads for comparison.

These analyses were specifically conducted for Araldite® AV138, as the contact status on nodes does not change for geometries without complete separation when using other adhesives. Fig. 11 reveals that geometries without complete separation were notably stronger than those undergoing complete separation. Noteworthy is the Edge Overhang geometry, exhibiting the highest strength, with the load at complete separation more than double that of the Block geometry.

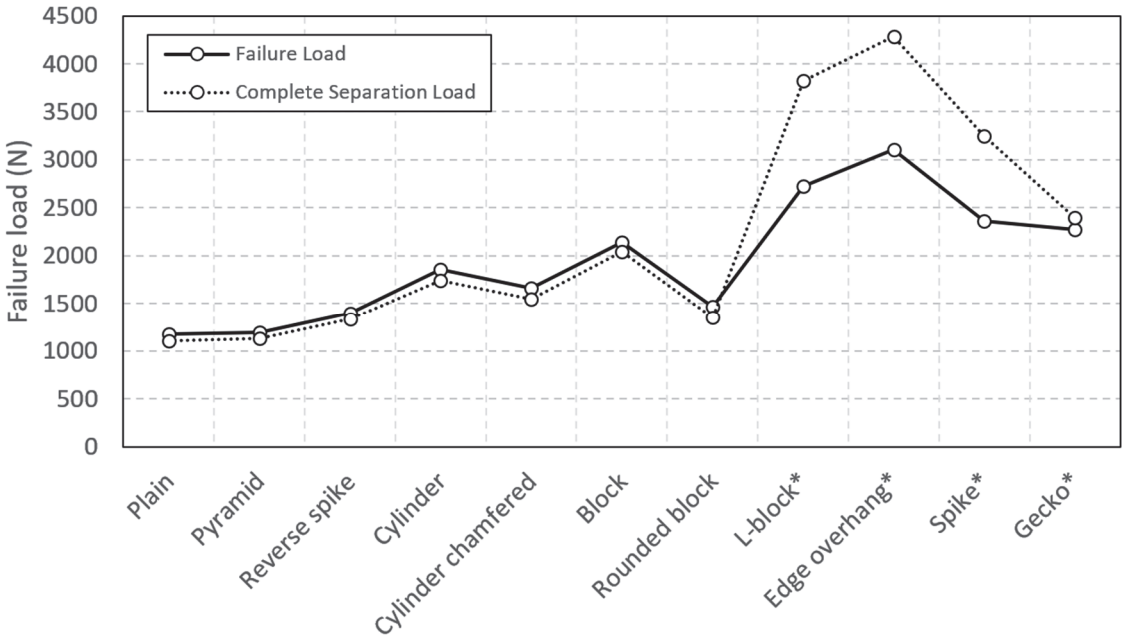

Figure 11: Failure loads comparison of different joints bonded with Araldite® AV138. (* joints which do not undergo complete separation)

CONCLUSIONS

This study focuses on the impact of various anchor geometries on the overall strength of joints, with a primary assumption underpinning the comparison: joint failure consistently occurs in cohesive or adhesive mode. Therefore, the comparison aims to identify the optimal geometry for potential cohesive failure within the joint. To facilitate this assessment, a relatively weak adhesive, Araldite AV138, was utilized as the bonding agent, facilitating complete separation of the adherents' touching surfaces and thereby allowing to disregard potential failure of the anchors or adherents. Nonetheless, as observed in the numerical study results, certain geometries, even with the selected adhesive, do not permit joints to undergo complete separation. In such cases, the possibility of anchor or adherent failure remains, a phenomenon documented in the literature for similar joints [16-19]. However, given that the comparison focuses on the contact status over the overlap region, failures of pins or adherents due to stress concentrations in these regions were excluded from consideration, as they do not align with the study's method of comparison.

This research evaluates the effectiveness of 3D anchors for metal and composite materials in joint strength enhancement. The primary focus is on investigating modified joint geometries using reliable numerical methods, particularly the CZM. Exploration of various geometries highlights their significant influence on joint strength. Modification of anchor geometry within SLJ adherents shows potential for altering joint failure resistance.

The CZM approach offers crucial insights into joint behavior, enhancing understanding of strength, separation initiation, anchor geometry impact, and contact status evolution. It provides flexibility in anchor design based on desired joint behavior and aids in selecting suitable geometries for specific applications. Moreover, designs enhancing mechanical interlocking demonstrate higher joint strength, with even slight geometric changes, such as anchor orientation, impacting joint strength significantly.

FUNDING

This paper was funded by the Horizon Europe grant "HORIZON-CL4-2022-RESILIENCE-01", Project MIMOSA (Project 101091826).

REFERENCES

[1] Khosravani, M.R., Soltani, P., Reinicke, T. (2021). Fracture and structural performance of adhesively bonded 3D-printed PETG single lap joints under different printing parameters, Theor. Appl. Fract. Mech., 116, pp. 103087, DOI: 10.1016/J.TAFMEC.2021.103087.

[2] Iwata, K., Suzuki, A., Kim, S.G., Takata, N., Kobashi, M. (2022). Enhancing the solid-state joinability of A5052 and CFRTP via an additively manufactured micro-structure, J. Mater. Process. Technol., 306, pp. 117629, DOI: 10.1016/J.JMATPROTEC.2022.117629.

[3] Nguyen, A.T.T., Brandt, M., Orifici, A.C., Feih, S. (2016). Hierarchical surface features for improved bonding and fracture toughness of metal–metal and metal–composite bonded joints, Int. J. Adhes. Adhes., 66, pp. 81–92, DOI: 10.1016/J.IJADHADH.2015.12.005.

[4] Parkes, P.N., Butler, R., Meyer, J., de Oliveira, A. (2014). Static strength of metal-composite joints with penetrative reinforcement, Compos. Struct., 118(1), pp. 250–6, DOI: 10.1016/J.COMPSTRUCT.2014.07.019.

[5] Neto, J.A.B.P., Campilho, R.D.S.G., Da Silva, L.F.M. (2012). Parametric study of adhesive joints with composites, Int. J. Adhes. Adhes., 37, pp. 96–101, DOI: 10.1016/J.IJADHADH.2012.01.019.

[6] Nash, R.J., Li, Y. (2021). Experimental and numerical analysis of 3D printed suture joints under shearing load, Eng. Fract. Mech., 253, pp. 107912, DOI: 10.1016/J.ENGFRACMECH.2021.107912.

[7] Ramaswamy, K., O'Higgins, R.M., Lyons, J., McCarthy, M.A., McCarthy, C.T. (2021). An evaluation of the influence of manufacturing methods on interlocked aluminium-thermoplastic composite joint performance, Compos. Part A Appl. Sci. Manuf., 143, pp. 106281, DOI: 10.1016/J.COMPOSITESA.2021.106281.

[8] Armentani, E., Laiso, M., Caputo, F., Sepe, R. (2018). Numerical FEM Evaluation for the Structural Behaviour of a Hybrid (bonded/bolted) Single-lap Composite Joint, Procedia Struct. Integr., 8, pp. 137–153, DOI: 10.1016/J.PROSTR.2017.12.015.

[9] Zhang, H., Zhang, L., Liu, Z., Qi, S., Zhu, Y., Zhu, P. (2021). Numerical analysis of hybrid (bonded/bolted) FRP composite joints: A review, Compos. Struct., 262, pp. 113606, DOI: 10.1016/J.COMPSTRUCT.2021.113606.

[10] De Pasquale, G., Coluccia, A. (2023). Modeling and Experimental Validation of CFRP-Metal Joints Utilizing 3D Additively Manufactured Anchors, J. Manuf. Sci. Eng., 145(11), DOI: 10.1115/1.4063110/1166161.

[11] De Pasquale, G., Enes Altunok, F., Ursi, F. (2023). Investigation of the Mechanical Strength of CFRP with Co-Cured Additively Manufactured Metal Inserts, Procedia Struct. Integr., 47, pp. 573–8, DOI: 10.1016/J.PROSTR.2023.07.067.

[12] Coluccia, A., Jiang, G., Meyer, G., De Pasquale, G., Mittelstedt, C. (2023). Nonlinear static and dynamic modeling of energy absorption lattice structures behavior, Mech. Adv. Mater. Struct., 30(14), DOI: 10.1080/15376494.2022.2064016.

[13] De Pasquale, G., Tagliaferri, A. (2021). Modeling and characterization of mechanical and energetic elastoplastic behavior of lattice structures for aircrafts anti-icing systems, Proc. Inst. Mech. Eng. Part C J. Mech. Eng. Sci., 235(10), pp. 1828–39, DOI: 10.1177/0954406219853857.

[14] Coluccia, A., De Pasquale, G. (2023). Strain-based method for fatigue failure prediction of additively manufactured lattice structures, Sci. Rep., 13(1), DOI: 10.1038/s41598-023-49846-z.

[15] Carvalho, U.T.F., Campilho, R.D.S.G. (2017). Validation of pure tensile and shear cohesive laws obtained by the direct method with single-lap joints, Int. J. Adhes. Adhes., 77, DOI: 10.1016/j.ijadhadh.2017.04.002.

[16] von H.P.F. Silva, M.T., Camanho, P.P., Marques, A.T., Castro, P.M.S.T. (2017). 3D-reinforcement techniques for co-bonded CFRP/CFRP and CFRP/metal joints: a brief review, Ciencia e Tecnologia Dos Materiais, 29(1), pp. e102–e107. DOI: 10.1016/j.ctmat.2016.07.011.

[17] Inverarity, S.B., Das, R., Mouritz, A.P. (2022). Composite-to-metal joining using interference fit micropins, Compos Part A Appl Sci Manuf, 156. DOI: 10.1016/j.compositesa.2022.106895.

[18] Sarantinos, N., Tsantzalis, S., Ucsnik, S., Kostopoulos, V. (2019). Review of through-the-thickness reinforced composites in joints, Compos Struct. DOI: 10.1016/j.compstruct.2019.111404.

[19] Wang, X., Ahn, J., Lee, J., Blackman, B.R.K. (2016). Investigation on failure modes and mechanical properties of CFRP-Ti6Al4V hybrid joints with different interface patterns using digital image correlation, Mater Des, 101, pp. 188–196. DOI: 10.1016/j.matdes.2016.04.005.